NEUROSCIENCE

Trisomy 21–induced dysregulation of microglial homeostasis in Alzheimer's brains is mediated by USP25

Qiuyang Zheng[1]*, Guilin Li[1]*, Shihua Wang[1,2], Ying Zhou[3], Ke Liu[3], Yue Gao[1], Yulin Zhou[4], Liangkai Zheng[4], Lin Zhu[1], Qingfang Deng[1], Meiling Wu[1], Anjie Di[1], Lishan Zhang[1], Yingjun Zhao[1], Hongfeng Zhang[1], Hao Sun[1], Chen Dong[5], Huaxi Xu[1,6], Xin Wang[1]†

Down syndrome (DS), caused by trisomy of chromosome 21, is the most significant risk factor for early-onset Alzheimer's disease (AD); however, underlying mechanisms linking DS and AD remain unclear. Here, we show that triplication of homologous chromosome 21 genes aggravates neuroinflammation in combined murine DS-AD models. Overexpression of *USP25*, a deubiquitinating enzyme encoded by chromosome 21, results in microglial activation and induces synaptic and cognitive deficits, whereas genetic ablation of *Usp25* reduces neuroinflammation and rescues synaptic and cognitive function in 5×FAD mice. Mechanistically, USP25 deficiency attenuates microglia-mediated proinflammatory cytokine overproduction and synapse elimination. Inhibition of USP25 reestablishes homeostatic microglial signatures and restores synaptic and cognitive function in 5×FAD mice. In summary, we demonstrate an unprecedented role for trisomy 21 and pathogenic effects associated with microgliosis as a result of the increased *USP25* dosage, implicating USP25 as a therapeutic target for neuroinflammation in DS and AD.

INTRODUCTION

Down syndrome (DS), which results from total or partial trisomy of chromosome 21, is the most common cause of intellectual disability, with an incidence of 1 in approximately 800 births worldwide (*1*, *2*). Trisomy 21 is the single most common risk factor for early-onset Alzheimer's disease (AD) (*3*). By the age of 40, individuals with DS universally develop neuropathological features associated with AD, including amyloid plaques, neurofibrillary tangles, synaptic dysfunction, and neuroinflammation in vulnerable brain regions (*4*, *5*). However, whether and how chromosome 21 genes influence AD pathogenesis in the context of DS remain largely unknown.

As the major immune cells in the brain, microglia play a key role in maintaining central nervous system (CNS) homeostasis and protecting the brain from infection and injury (*6*, *7*). Microglia transition to a reactive state associated with enhanced proinflammatory cytokine secretion and phagocytic uptake during injury (*8*–*10*). Short-term activation of microglia may facilitate debris clearance and tissue repair (*11*, *12*); however, sustained activation of microglia induces chronic release of proinflammatory cytokines, thereby initiating inflammatory cascades and pathogenic neurotoxic effects in neurodegeneration (*13*–*15*).

The ubiquitin-proteasome system (UPS) is an essential protein degradation pathway (*16*), and defects in the UPS induce the accumulation of neurotoxic proteins in various neurodegenerative disorders, such as AD, Parkinson's disease, and Huntington's disease (*17*). The *USP25* gene is located on human chromosome 21q11.2 and encodes the ubiquitin-specific protease ubiquitin-specific peptidase 25 (USP25) (*18*). USP25 was first identified as a negative regulator of interleukin-17 (IL-17)–mediated signaling and the inflammatory response (*19*). In addition, USP25 deficiency inhibits transcriptional activity of interferon regulatory factor, thereby reducing type I interferon production (*20*). UPS-mediated protein degradation and neuroinflammation play an important role in neurodegeneration; however, the contribution of USP25 in the pathogenesis of DS and AD remains unclear.

Here, we show that an extra copy of chromosome 21 aggravates neuroinflammation in 5×FAD mice and that the DS-related gene *USP25* plays a key role in this process. Bacterial artificial chromosome (BAC)–Tg–USP25 mice displayed neuropathologies resembling those exhibited by DS-AD mice, including microglial activation and impaired synaptic and cognitive function. In addition, genetic deletion of *Usp25* in 5×FAD mice markedly attenuated neuroinflammation and cognitive deficits. Pharmacological treatment with USP25 inhibitors restored microglia to a homeostatic transcriptional state and reversed impairments in synaptic and cognitive function in 5×FAD mice. Therefore, our investigation revealed a critical role for USP25 in maintaining microglial homeostasis in neurodegeneration and identified a novel therapeutic avenue for AD and DS.

RESULTS

Trisomy of chromosome 21 genes promotes neuroinflammation

To investigate whether triplication of chromosome 21 genes alters AD pathogenesis, we generated a DS-AD mouse model by crossing the Dp16 DS mouse model (*21*, *22*) with 5×FAD mice (*23*). We performed whole-genome RNA sequencing (RNA-seq) and subsequent consensus weighted gene coexpression network analyses (WGCNAs) on hippocampal tissue from wild-type (WT), Dp16, 5×FAD, and

[1]State Key Laboratory of Cellular Stress Biology, Fujian Provincial Key Laboratory of Neurodegenerative Disease and Aging Research, Institute of Neuroscience, School of Medicine, Xiamen University, Xiamen, Fujian 361005, China. [2]School of Medicine, Xizang Minzu University, Xianyang, Shaanxi 712082, China. [3]Department of Translational Medicine, School of Medicine, Xiamen University, Xiamen, Fujian 361005, China. [4]Women and Children's Hospital, School of Medicine, Xiamen University, Xiamen, Fujian 361003, China. [5]Institute for Immunology, School of Medicine, Tsinghua University, Beijing 100084, China. [6]Center for Brain Sciences, The First Affiliated Hospital of Xiamen University, School of Medicine, Xiamen University, Xiamen, Fujian 361003, China.
*These authors contributed equally to this work.
†Corresponding author. Email: wangx@xmu.edu.cn

5×FAD;Dp16 mice and identified 14 coexpression modules (Fig. 1A). By correlating eigengenes to corresponding genotypes, we found that three modules (M3, M4, and M5) were significantly up-regulated in 5×FAD;Dp16 versus 5×FAD mice (Fig. 1A). Gene Ontology (GO) enrichment analysis revealed that genes within the M3 module (1641 genes) were implicated in pathways related to "cytokine production," "microglial activation," and "phagocytosis" (Fig. 1B). Moreover, the expression of microglia-related genes was up-regulated by triplication of murine chromosome 16 (homologous to human chromosome 21) in 5×FAD;Dp16 mice compared with 5×FAD alone (Fig. 1C).

Consistent with the transcriptomic profiles, we observed Iba1+ microglial proliferation and activation in hippocampus and cortex from Dp16 and 5×FAD mice (Fig. 1, D to H, and fig. S1, A to E). DS-associated chromosome 16 triplication also enhanced microglial proliferation and activation in 5×FAD;Dp16 mouse brain compared with Dp16 and 5×FAD mouse brain (Fig. 1, D to H, and fig. S1, A to G).

We then searched for microglia-related differentially expressed genes (DEGs) encoded on chromosome 21 (mouse chromosome 16) that were associated with inflammation and identified *USP25* as a
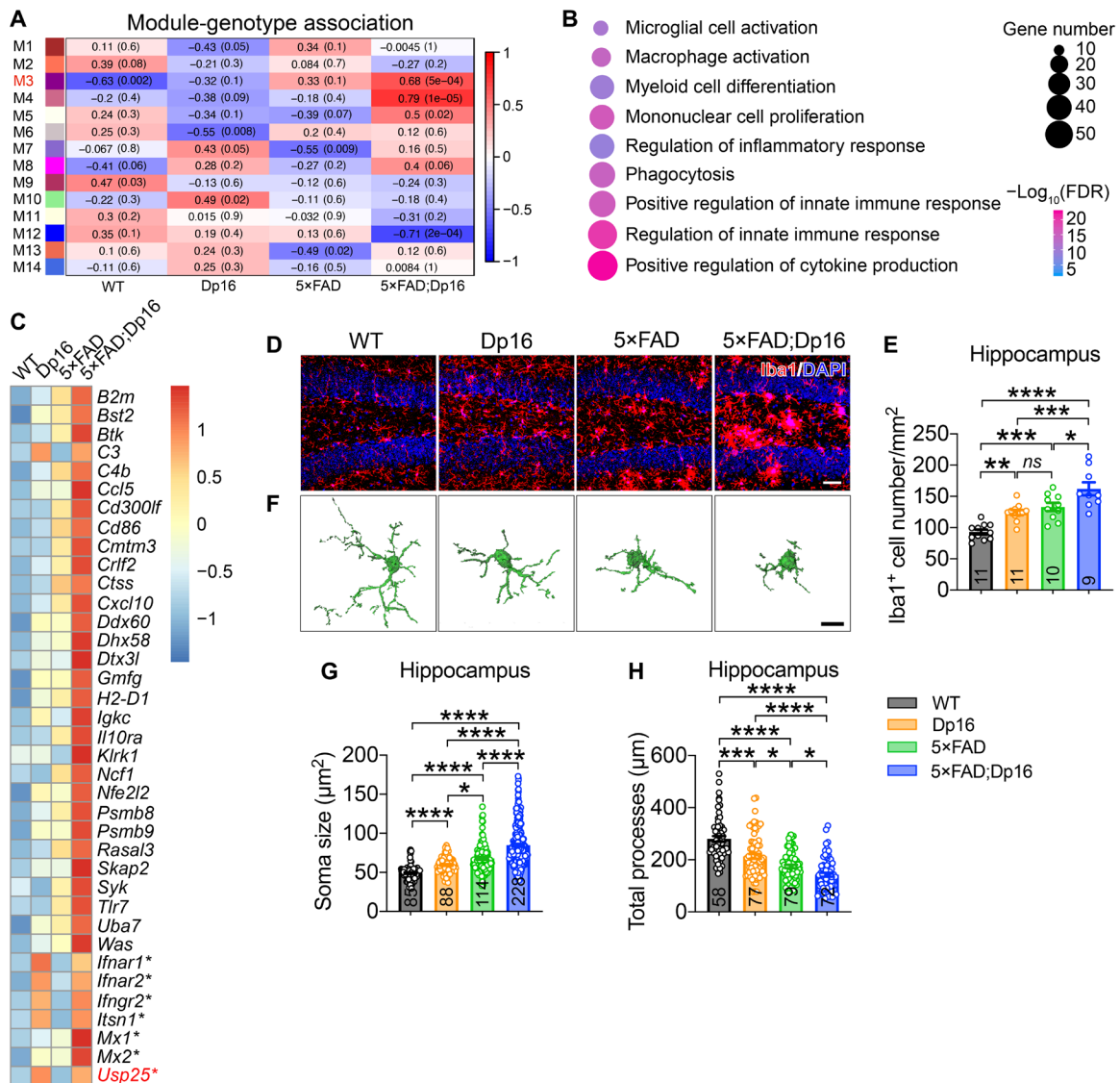

Fig. 1. Trisomy of chromosome 21 genes promotes neuroinflammation. (**A** to **C**) Transcriptome analysis of 5-month-old WT, Dp16, 5×FAD, and 5×FAD;Dp16 mice. $n = 6$ mouse hippocampi. (A) WGCNA analysis of module eigengenes. Rows correspond to modules, and columns correspond to genotypes. Numbers in the heatmap represent Z statistics and corresponding P values of the module eigengene association with the indicated genotypes. (B) GO analysis of M3 genes. (C) Heatmap depicting microglia-related genes that were up-regulated in 5×FAD;Dp16 versus 5×FAD mouse hippocampus. The asterisk indicates homologous genes on human chromosome 21. (**D** and **E**) Representative immunostaining (D) and quantification of Iba1+ microglia (E) in 5-month-old WT, Dp16, 5×FAD, and 5×FAD;Dp16 mouse hippocampus. Scale bar, 40 μm. $n = 5$ to 6 mice per group; $n = 9$ to 11 slices per group were scored. (**F**) Representative 3D reconstruction of Iba1+ microglia using Imaris software. Scale bar, 10 μm. (**G** and **H**) Quantification of microglial soma size (G) and total processes (H). $n = 4$ to 6 mice per group; $n = 58$ to 228 microglia per group were counted. All data represent means ± SEM. P values were determined by one-way ANOVA with Tukey's post hoc analysis in (E) and by the Kruskal-Wallis test with Dunn's post hoc analysis in (G) and (H). ns, not significant. *$P < 0.05$; **$P < 0.01$; ***$P < 0.001$; ****$P < 0.001$.

potential gene candidate. USP25 was up-regulated in the brains of both human DS patients (fig. S1, H and I) and Dp16 mice (fig. S1, J and K). USP25 is a deubiquitinase that was previously implicated in innate immunity (*19*). Our previous results indicate that USP25 is ubiquitously expressed in different cell types in the CNS, and show markedly high expression in microglia and astrocytes (fig. S1, L and M).

To mimic USP25 overexpression in DS in a transgenic mouse model, we used a human *USP25* BAC transgenic approach (fig. S2, A and B). To address whether the increased *USP25* gene dosage may alter disease-associated microglial function and other AD-related phenotypes, we crossed BAC-Tg-USP25 with 5×FAD mouse lines. We first assessed cognitive function in 5-month-old 5×FAD;BAC-Tg-USP25 mice (early phase of disease progression) using the Y-maze spontaneous alternation task; we observed that 5×FAD;BAC-Tg-USP25 mice displayed impaired spatial memory compared with WT and 5×FAD mice (Fig. 2A). The dendritic spine density in hippocampal neurons was reduced in 5×FAD;BAC-Tg-USP25 compared with 5×FAD mice (Fig. 2B). To confirm whether *USP25* overdosage impairs synaptic function, we measured long-term potentiation (LTP) in hippocampal Schaffer collaterals and observed marked LTP impairment in BAC-Tg-USP25, 5×FAD, and 5×FAD;BAC-Tg-USP25

compared with WT mice (Fig. 2, C and D). Furthermore, we observed microglial proliferation and activation in the hippocampus and cortex in BAC-Tg-USP25 and 5×FAD mice (Fig. 2, E to I, and fig. S2, C to I). Moreover, USP25 overexpression further boosted microglial proliferation and activation in 5×FAD;BAC-Tg-USP25 mouse brain (Fig. 2, E to I, and fig. S2, C to I). Together, these results demonstrate that USP25 overexpression phenocopies pathogenic effects associated with DS chromosome 21 triplication.

Genetic deletion of *Usp25* reverses cognitive and synaptic deficits in AD mice

To determine the effects of *Usp25* deficiency on AD-related cognitive dysfunction, we assayed learning and memory behavior in 5×FAD;*Usp25*^{+/−} mice (fig. S3A). Compared with 5×FAD mice, 5×FAD;*Usp25*^{+/−} mice displayed improved spatial memory in the Y-maze (Fig. 3A) and Morris water maze (MWM) tests (Fig. 3, B and C), as well as improved associative memory in fear conditioning (FC) tests (Fig. 3, D and E). Dendritic spine density was also found to be increased in 5×FAD;*Usp25*^{+/−} compared with 5×FAD mouse hippocampus (Fig. 3F). To determine whether *Usp25* deficiency restores synaptic function in 5×FAD mice, we measured hippocampal LTP and found that it was compromised in 5×FAD compared with
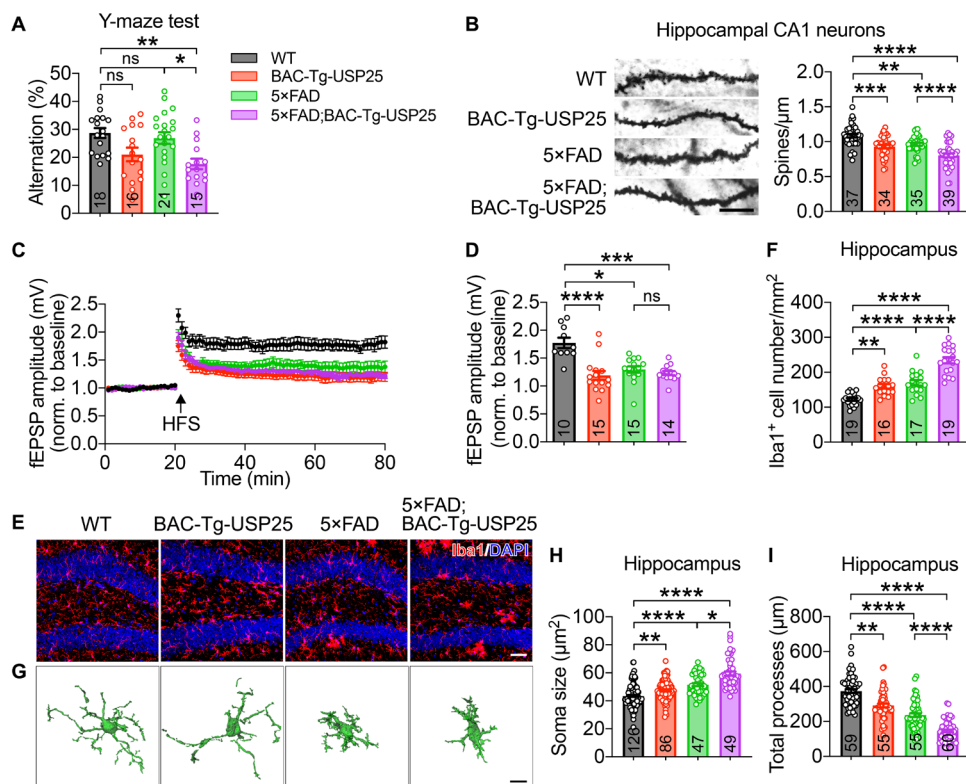

Fig. 2. Overexpression of USP25 promotes synapse loss and microglial activation in AD mice. (**A**) Percentage of spontaneous alternation in the Y-maze. *n* = 15 to 21 5-month-old mice per group. (**B**) Golgi staining and quantification of dendritic spines in the hippocampal CA1 regions of 6-month-old WT, BAC-Tg-USP25, 5×FAD, and 5×FAD;BAC-Tg-USP25 mice. Scale bar, 10 μm. *n* = 4 mice per group; *n* = 34 to 39 dendrites per group were counted. (**C**) Hippocampal CA1 LTP recordings from 6-month-old mice. HFS, high-frequency stimulation. (**D**) fEPSP amplitude quantification during the last 10 min of LTP recording. WT (*n* = 5 mice, 10 slices), BAC-Tg-USP25 (*n* = 5 mice, 15 slices), 5×FAD (*n* = 7 mice, 15 slices), and 5×FAD;BAC-Tg-USP25 (*n* = 5 mice, 14 slices). (**E** and **F**) Representative immunostaining (E) and quantification of Iba1^{+} microglia (F) in 6-month-old WT, BAC-Tg-USP25, 5×FAD, and 5×FAD;BAC-Tg-USP25 mouse hippocampus. Scale bar, 40 μm. *n* = 5 to 7 mice per group; *n* = 16 to 19 slices per group were scored. (**G**) Representative 3D reconstruction of Iba1^{+} microglia. Scale bar, 8 μm. (**H** and **I**) Quantification of microglial soma size (H) and total processes (I). *n* = 3 to 5 mice per group; *n* = 47 to 126 microglia per group were counted. All data represent means ± SEM. *P* values were determined by one-way ANOVA with Tukey's post hoc analysis in (A), (B), and (F) and by the Kruskal-Wallis test with Dunn's post hoc analysis in (D), (H), and (I). ns, not significant. *P < 0.05; **P < 0.01; ***P < 0.001; ****P < 0.001.
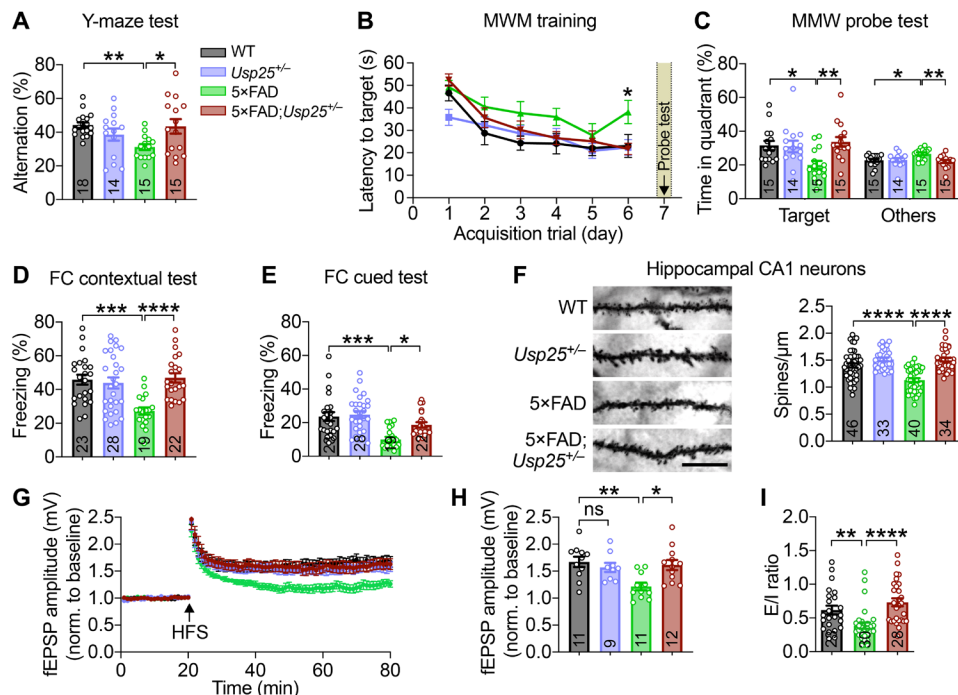
Fig. 3. Genetic deletion of *Usp25* enhances synaptic and cognitive function in AD mice. (**A**) Percentage of spontaneous alternation in the Y-maze. $n = 14$ to 18 6- to 7-month-old mice per group. (**B**) MWM test results depicting escape latency, defined as the time taken to find a hidden platform. (**C**) MWM probe test results. $n = 14$ to 15 6- to 7-month-old mice per group. (**D**) Percentage freezing time in contextual FC tests, as a readout of associative memory. (**E**) Percentage freezing time spent in cued FC tests. $n = 19$ to 28 6- to 7-month-old mice per group. (**F**) Golgi staining and quantification of dendritic spines in 9-month-old mouse hippocampus. Scale bar, 10 μm. $n = 4$ mice per group; $n = 33$ to 46 dendrites per group were counted. (**G**) Hippocampal CA1 LTP recordings from 6- to 7-month-old mice. HFS, high-frequency stimulation. (**H**) Quantification of the last 10 min of LTP recording. WT ($n = 6$ mice, 11 slices), *Usp25*^{+/−} ($n = 5$ mice, 9 slices), 5×FAD ($n = 5$ mice, 11 slices), and 5×FAD;*Usp25*^{+/−} ($n = 6$ mice, 12 slices). (**I**) Excitation/inhibition (E/I) ratio of hippocampal DG granule cells. $n = 4$ mice per group; $n = 23$ to 30 cells. All data represent means ± SEM. P values were determined by the Kruskal-Wallis test with Dunn's post hoc analysis in (A), (C) to (F), (H), and (I) and by repeated-measures ANOVA with Tukey's post hoc analysis in (B). ns, not significant. *$P < 0.05$; **$P < 0.01$; ***$P < 0.001$; ****$P < 0.0001$.

WT and *Usp25*^{+/−} mice; however, 5×FAD-associated LTP impairment was reversed in 5×FAD;*Usp25*^{+/−} mice (Fig. 3, G and H). Consistent with changes in dendritic spine density and LTP, *Usp25* deficiency reduced the miniature inhibitory postsynaptic current (mIPSC) frequency (fig. S3B) and increased the miniature excitatory postsynaptic current (mEPSC) frequency (fig. S3C) in hippocampal granule neurons in 5×FAD mice. Together, these results indicate that disruptions in excitation/inhibition signaling in 5×FAD mouse hippocampus can be restored by *Usp25* haploinsufficiency (Fig. 3I), and demonstrate that USP25 down-regulation reverses synaptic and cognitive deficits in 5×FAD mice.

USP25 deficiency reduces neuroinflammation in AD mouse brain

To further identify molecular networks that may be selectively targeted by *Usp25* deficiency, we performed RNA-seq and subsequent WGCNA analysis on the hippocampi of mice from four groups (WT, *Usp25*^{+/−}, 5×FAD, and 5×FAD;*Usp25*^{+/−}) and identified 16 co-expression modules (fig. S4A). Among these modules, M14 was significantly up-regulated in 5×FAD compared with WT and was partially restored in 5×FAD;*Usp25*^{+/−} mice (fig. S4A). GO enrichment analysis revealed that 4375 genes within the M14 module were implicated in "inflammatory response," "cytokine production," and "phagosome" pathways (Fig. 4A). Moreover, expression of microglia-related 5×FAD DEGs was restored by *Usp25* haploinsufficiency

in 5×FAD;*Usp25*^{+/−} mice (fig. S4B). In addition, we found that *Usp25* haploinsufficiency suppressed mRNA expression of proinflammatory cytokines *Il6* and *Tnf* in 5×FAD mouse hippocampus (fig. S4C).

Consistent with our transcriptomic analyses, genetic deletion of *Usp25* in a 5×FAD background suppressed Iba1^{+} microglial proliferation (Fig. 4, B and C, and fig. S4, D and E). Quantitative morphometric analysis revealed that 5×FAD microglia featured an increased soma size and reduced branch complexity and that these morphogenic changes were reversed with *Usp25* haploinsufficiency (Fig. 4, D to F, and fig. S4, F to H). In addition, quantification of the PSD95^{+} puncta volume internalized in Iba1^{+} microglia suggested that *Usp25* haploinsufficiency attenuated microglia-mediated engulfment of synapses in 5×FAD mouse brain (Fig. 4, D and G, and fig. S4, F and I). To confirm the effects of USP25 in AD-associated microglial dysfunction, we performed in vitro phagocytosis assays using cultured primary microglia and pH-sensitive dye-labeled synaptosomes. We found that oligomeric Aβ42 (oAβ42) treatment markedly increased phagocytosis of synaptosomes in *Usp25*^{+/+}, but not in *Usp25*^{−/−}, microglia (fig. S4, J and K). To further determine whether *Usp25* deficiency affects clustering of microglia in vivo, we stereotactically injected oAβ42 into hippocampus of adult *Usp25*^{+/+} and *Usp25*^{−/−} mice and quantified the number of microglia proximal to oAβ42. oAβ42 increased the accumulation of activated microglia around the injection site in *Usp25*^{+/+} mouse brain; however, microglia largely failed to home to oAβ42 in *Usp25*^{−/−} mice (Fig. 4, H and I).
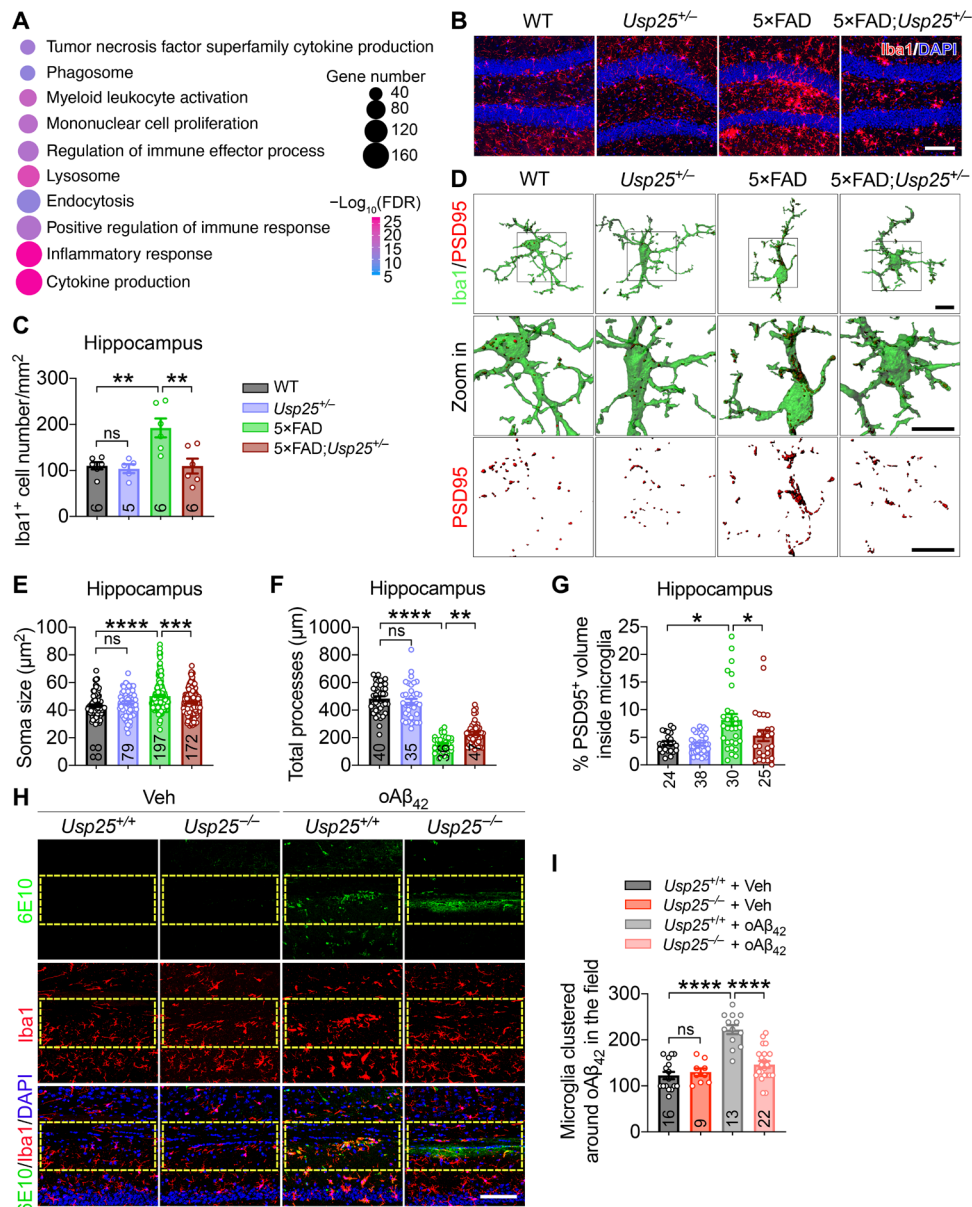
Fig. 4. *Usp25* haploinsufficiency restores microglial homeostasis. (**A**) GO analysis of M14 genes in fig. S4A. (**B** and **C**) Representative immunostaining (B) and quantification of Iba1$^+$ microglia (C) in 6- to 7-month-old WT, *Usp25$^{+/-}$*, 5×FAD, and 5×FAD;*Usp25$^{+/-}$* mouse hippocampus. Scale bar, 100 μm. n = 5 to 6 mice per group. (**D**) Representative 3D reconstruction and rendering of PSD95 puncta internalized in Iba1$^+$ microglia (PSD95/Iba1). Scale bar, 10 μm. (**E** to **G**) Quantification of microglial soma size (E), total processes (F), and percentage of PSD95$^+$ volume within microglia (G) in (D). n = 3 to 6 mice per group; n = 24 to 197 microglia per group were counted. (**H**) Representative immunostaining of oAβ$_{42}$-expressing regions in 7-month-old *Usp25$^{+/+}$* and *Usp25$^{-/-}$* mouse brain 16 hours after oAβ$_{42}$ injection. Scale bar, 100 μm. (**I**) Quantification of Iba1$^+$ microglia clustered in oAβ$_{42}$-expressing regions. n = 3 mice per group; n = 9 to 22 fields [selected area with yellow lines in (H)] were quantified. All data represent means ± SEM. P values were determined by one-way ANOVA with Tukey's post hoc analysis in (C), (F), and (I) and by the Kruskal-Wallis test with Dunn's post hoc analysis in (E) and (G). ns, not significant. *$P < 0.05$; **$P < 0.01$; ***$P < 0.001$; ****$P < 0.0001$.

USP25 deficiency increases proteasomal degradation of WDFY1 and ATP6V0C

To determine the underlying molecular mechanism by which USP25 regulates microglial function, we characterized protein expression profiles from WT, 5×FAD, and 5×FAD;*Usp25$^{-/-}$* mouse cerebrum using tandem mass tag (TMT)–based quantitative proteomics. We identified 192 up-regulated and 193 down-regulated differentially expressed proteins (DEPs; fold change > 1.1; $P < 0.05$) in 5×FAD;

Usp25$^{-/-}$ relative to those in 5×FAD mouse brain (Fig. 5A). WDFY1 and ATP6V0C were the top down-regulated proteins identified by proteomic analysis (Fig. 5A). GO enrichment analysis revealed an enrichment of proteins related to the immune system and neuroinflammation among the down-regulated DEPs (Fig. 5B), as well as neuroinflammation and learning/memory-related pathways among the up-regulated DEPs (fig. S5A). Given that USP25 is a deubiquitinase, down-regulated DEPs in response to *Usp25* deletion such as
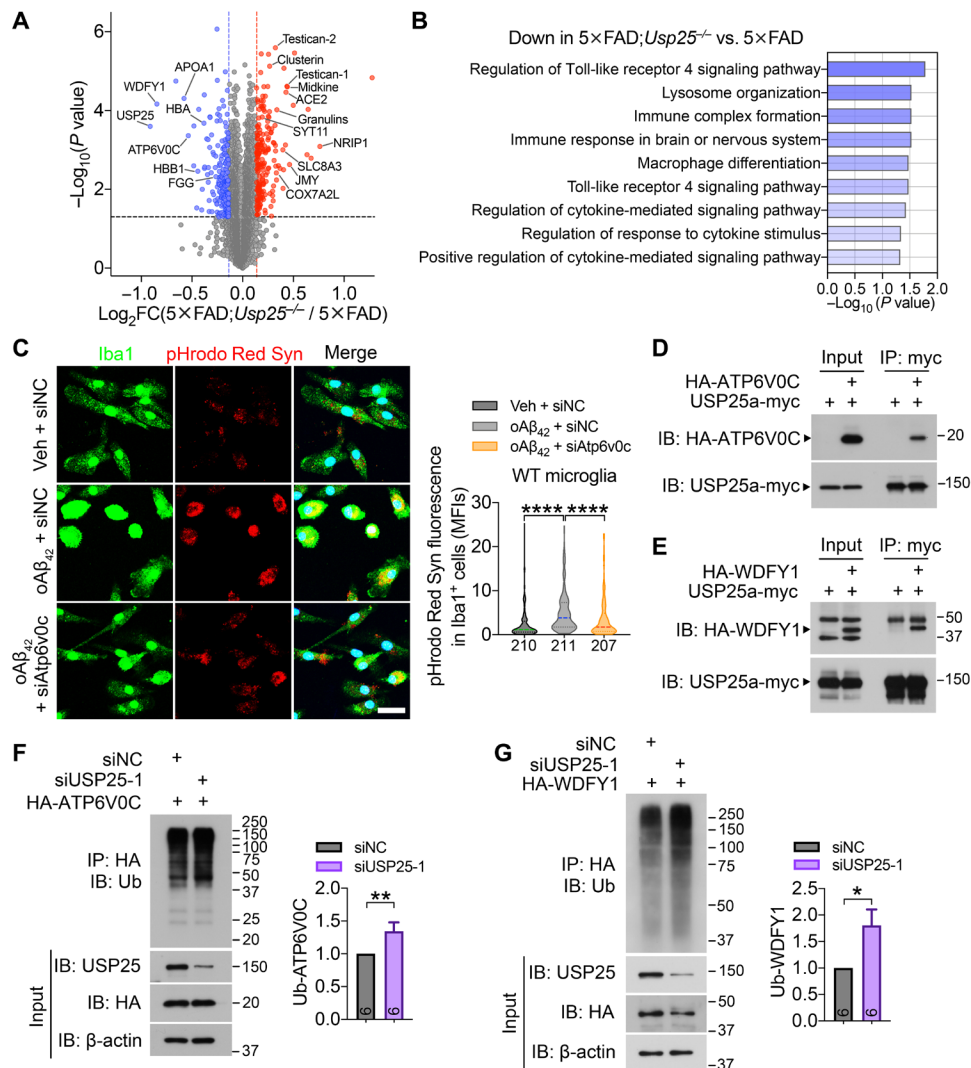
Fig. 5. USP25 deubiquitinates and stabilizes WDFY1 and ATP6V0C. (A and **B**) Quantitative proteomic analysis of the mouse cerebrum. (A) Proteomic analysis of the mouse cerebrum and a volcano plot illustrating down-regulated (blue) and up-regulated (red) proteins in the cerebra of 6-month-old 5×FAD;$Usp25^{-/-}$ versus 5×FAD mice (fold change > 1.1, $P < 0.05$). $n = 3$ samples per group; each sample is a pool of three cerebra from the same genotype. (B) GO analysis of down-regulated proteins in 5×FAD;$Usp25^{-/-}$ mice relative to 5×FAD mice. (**C**) Primary microglia from WT mice were transfected with siAtp6v0c or control siRNA (siNC) for 48 hours and subsequently treated with 10 μM oAβ42 or vehicle control along with pHrodo Red–labeled synaptosomes (Syn) for another 24 hours, and the phagocytosis abilities of microglia were quantified on the basis of the pHrodo Red intensity in Iba1+ cells. Scale bar, 25 μm. $n = 3$ independent experiments; $n = 207$ to 211 cells per group were counted. (**D** and **E**) Coimmunoprecipitation (IP) between exogenously expressed USP25a-myc and HA-ATP6V0C (D) or HA-WDFY1 (E) proteins. (**F** and **G**) Immunoblot (IB) analysis of poly-ubiquitinated HA-ATP6V0C (F) and HA-WDFY1 (G) in HEK293T cells upon USP25 knockdown. $n = 6$. All data represent means ± SEM. P values were determined by the Kruskal-Wallis test with Dunn's post hoc analysis in (C) and by the Mann-Whitney test in (F) and (G). *$P < 0.05$; **$P < 0.01$; ****$P < 0.0001$.

WDFY1 and ATP6V0C could potentially represent USP25 targets. WDFY1 and ATP6V0C have been previously implicated in inflammation and pathways associated with lysosomal function. WDFY1 promotes Toll-like receptor 3 (TLR3)– and TLR4-mediated activation of nuclear factor κB (NF-κB) and enhances inflammatory cytokine production (24). Our results indicated that depletion of ATP6V0C markedly attenuated oAβ42-induced microglial phagocytosis of synaptosomes (Fig. 5C and fig. S5B). We further verified the colocalization between USP25 and ATP6V0C or WDFY1 by immunocytochemistry (fig. S5, C and D) and their interaction with USP25 by coimmuno-precipitation (Fig. 5, D and E). We demonstrated that USP25 knockdown reduced HA-ATP6V0C and HA-WDFY1 expression (fig. S5, E and F) and increased polyubiquitinated HA-ATP6V0C and HA-

WDFY1 levels (Fig. 5, F and G). We next found that enhanced ATP6V0C and WDFY1 degradation associated with USP25 depletion was reversed by inhibition of proteasomal protein degradation and, to a smaller extent, by inhibition of lysosomal protein degradation (fig. S5, G and H).

USP25 inhibition ameliorates neurological dysfunction in AD mice

To assess the functional role of USP25 inhibition in vivo, we evaluated the pharmacokinetic properties of the USP25 inhibitor AZ1 in mice (Fig. 6A) (25). We found that at 0.5 hour after a single administration of AZ1 by intragastric gavage, AZ1 reached a maximum concentration in the brain that was maintained for up to 8 hours
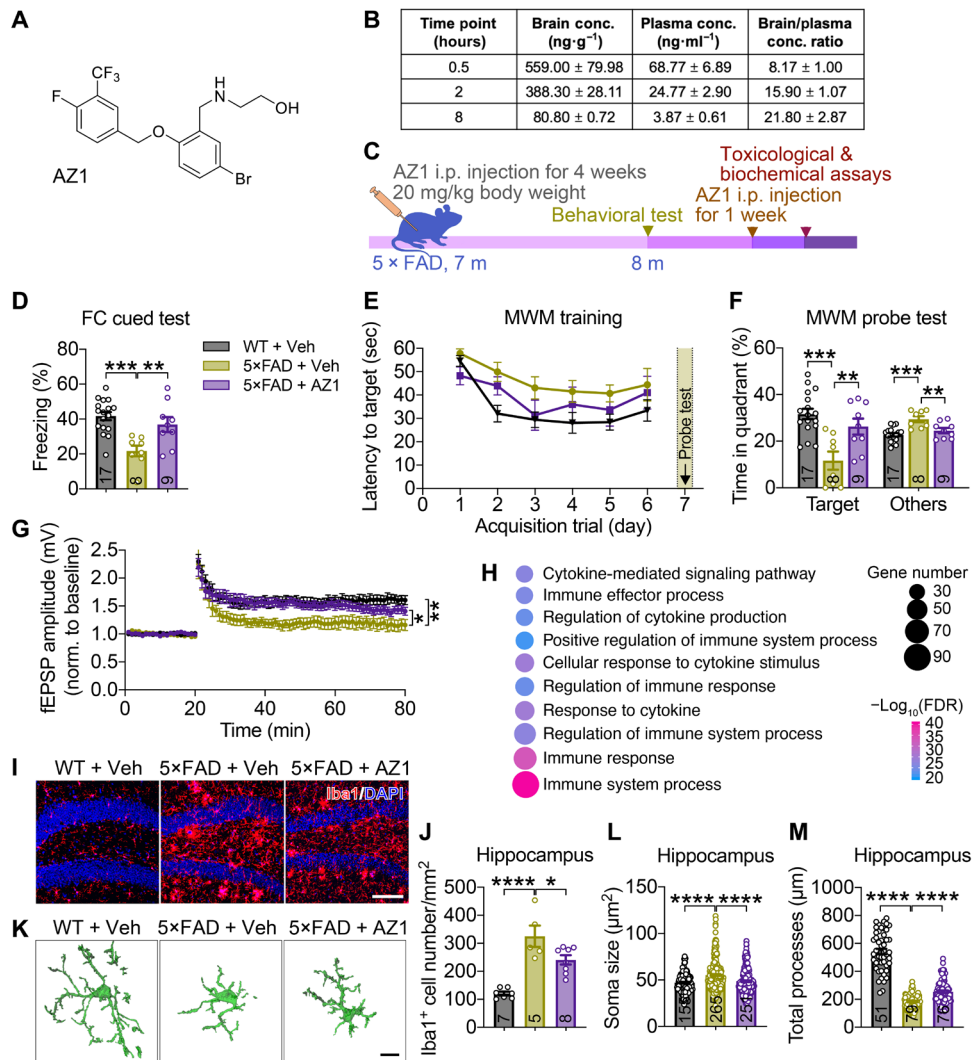
Fig. 6. USP25 inhibition ameliorates AD-related impairments in 5×FAD mice. (**A**) Chemical structure of AZ1. (**B**) Brain concentrations of AZ1 detected by LC-MS/MS after intragastric gavage at body weight (10 mg kg^{-1}). (**C**) Timeline of the AZ1 injection experiments. Three treatment groups in this study included the following: WT + vehicle, 5×FAD + vehicle, and 5×FAD + AZ1 groups. Seven-month-old mice were intraperitoneally (i.p.) injected with vehicle or AZ1 (20 mg kg^{-1} day^{-1}) for 4 weeks and subjected to behavioral and pathological analyses. (**D**) Characterizing therapeutic effects associated with AZ1 on cued fear memory. WT + vehicle ($n = 17$ mice), 5×FAD + vehicle ($n = 8$ mice), and 5×FAD + AZ1 ($n = 9$ mice). (**E**) Escape latency in MWM tests. (**F**) MWM probe test results. (**G**) Hippocampal CA1 LTP recordings and quantification of the last 10 min of the LTP recording. WT + vehicle ($n = 5$ mice, 10 slices), 5×FAD + vehicle ($n = 4$ mice, 7 slices), and 5×FAD + AZ1 ($n = 7$ mice, 12 slices). (**H**) GO analysis of overlapping genes in fig. S7A. (**I** and **J**) Representative immunostaining (I) and quantification of Iba1$^+$ microglia (J) in WT + vehicle, 5×FAD + vehicle, and 5×FAD + AZ1 mouse hippocampus. Scale bar, 100 μm. $n = 5$ to 8 mice per group. (**K**) Representative 3D reconstruction of Iba1$^+$ microglia. Scale bar, 10 μm. (**L** and **M**) Quantification of microglial soma size (L) and total processes (M). $n = 5$ mice per group; $n = 51$ to 265 microglia per group were counted. All data represent means ± SEM. P values were determined by one-way ANOVA with Dunnett's post hoc analysis in (D), (F), (J), (L), and (M); by repeated-measures ANOVA with Tukey's post hoc analysis in (E); and by one-way ANOVA with Holm-Sidak's post hoc analysis in (G). *$P < 0.05$; **$P < 0.01$; ***$P < 0.001$; ****$P < 0.001$.

(Fig. 6B). Subchronic administration of AZ1 (20 mg kg^{-1}) did not show any apparent toxic effects, as indicated by body weight gain (Fig. 6C and fig. S6A) and metabolic profiling (fig. S6, B to L). Subchronic injection of AZ1 in 5×FAD mice markedly ameliorated memory deficits in cued FC (Fig. 6D) and MWM tests (Fig. 6, E and F). In addition, we measured hippocampal LTP and found that LTP impairment was reversed through long-term AZ1 administration (Fig. 6G).

We next investigated the mechanisms underlying AZ1-dependent neuroprotection through transcriptomic profiling in 5×FAD animals treated with AZ1. A total of 2349 genes were up-regulated in the 5×FAD hippocampus compared with the WT hippocampus (fold change > 1.2; $P < 0.05$); among up-regulated DEGs identified, expression of 446 genes was partially restored with AZ1 (fig. S7A). GO analysis revealed that genes implicated in immune- and inflammation-related pathways were enriched in 5×FAD DEGs restored with AZ1 treatment (Fig. 6H), with a large number of DEGs featuring microglia-specific expression (fig. S7B). In addition, AZ1 suppressed the expression of proinflammatory cytokines *Il1b* and *Il6* in 5×FAD mouse hippocampus, as quantified by quantitative reverse transcription polymerase chain reaction (qRT-PCR) (fig. S7C). Consistent with our transcriptomic analysis, we found that AZ1 administration

attenuated microglial proliferation and activation in the hippocampus (Fig. 6, I to M) and cortex (fig. S7, D to H) of 5×FAD mice. To validate whether AZ1 regulates microglial function in a USP25-dependent manner, we treated $Usp25^{+/+}$ and $Usp25^{-/-}$ microglia with AZ1 and found that AZ1 markedly attenuated oAβ$_{42}$-induced phagocytosis of synaptosomes in $Usp25^{+/+}$ microglia, with little or no effect in $Usp25^{-/-}$ microglia (fig. S7, I and J). Together, these results indicated that AZ1 ameliorated AD neuropathology by attenuating microglial activation.

DISCUSSION
Emerging evidence supports a pivotal role for innate immunity and neuroinflammation in DS and AD (26–30). Here, we show that a key component of UPS, USP25, is a critical regulator of CNS immune homeostasis in DS and AD. Overexpression of human USP25 recapitulated major neurological phenotypes in 5×FAD;Dp16 mice, including neuroinflammation and microglial activation. In addition, either genetic ablation or pharmacological inhibition of USP25 reversed neuroinflammatory, synaptic, and cognitive deficits in 5×FAD mice through restoration of microglial homeostasis. Prolonged USP25 inhibition restored proinflammatory transcriptional signatures associated with AD microglia and enhanced cognitive function in 5×FAD mice.

Although our focus here characterized a role for microglial USP25 in neurodegeneration, USP25 is known to be widely expressed in the CNS and peripheral nervous system (31). Our results using cultured microglia from $Usp25$ knockout mice showed that USP25 deficiency attenuated Aβ-induced phagocytosis of synapses, implicating a crucial role for USP25 in microglia-dependent synaptic uptake. However, there is still a possibility that USP25 in other cell types in the brain may also affect the CNS. Future studies characterizing the effects of conditional $Usp25$ deletion in various cell types will be required to decipher cell type–specific effects of USP25 perturbation in the CNS. Triplication of human chromosome 21 genes has been found to promote Aβ burden in a mouse model of DS-AD independently of an extra copy of APP (32). In addition to APP and $USP25$, the contribution of several chromosome 21–encoded genes and noncoding RNAs to AD pathogenesis has been reported, e.g., transcription factor $ETS2$ (33), small ubiquitin-related modifier 3 ($SUMO3$) (34), dual-specificity tyrosine-phosphorylation regulated kinase 1 A ($DYRK1A$) (35), β-site APP-cleaving enzyme 2 ($BACE2$) (36), cysteine protease cathepsin B ($CSTB$) (37), and microRNA miR-155 (38). Therefore, whether other chromosome 21 genes, individually or together with USP25, contribute to neuroinflammation in AD/DS pathogenesis remains to be further determined.

Multiple mechanisms may contribute to the protective effects associated with USP25 deficiency in 5×FAD mice. The induced proinflammatory cytokines TNFα (tumor necrosis factor α), IL-1β, and IL-6 are potentially neurotoxic and likely induce downstream neurodegenerative pathways (39, 40). Thus, suppression of cytokine production in the AD brain may inhibit neuroinflammation and associated pathogenic effects (41, 42). In addition, enhanced synaptic function may be directly attributed to decreased synaptic uptake in pathogenically activated microglia in AD brain. Our proteomic analysis identified WDFY1 and ATP6V0C as substrates of USP25. It has been reported that WDFY1 promotes TLR3- and TLR4-mediated activation of NF-κB and inflammatory cytokine production (24). We also found that depletion of ATP6V0C markedly attenuated

microglia-mediated phagocytosis of synapses. Together, these results indicate that USP25 deficiency suppresses microglia-mediated proinflammatory cytokine production and synapse elimination by targeting WDFY1 and ATP6V0C, respectively (fig. S8).

In conclusion, our results establish a critical role for USP25 in reprogramming microglial homeostasis in AD and DS. Given that ubiquitination and neuroinflammation have been found to play a crucial role in neurodegenerative disorders, further investigation of the function of USP25 may provide insights into therapeutic strategies to prevent or treat various neurodegenerative diseases through the restoration of microglial homeostasis.

MATERIALS AND METHODS
Study design
This study was performed to explore the underlying mechanism of chromosome 21–encoded deubiquitinase USP25 in the pathogenesis of AD, especially to verify the therapeutic potential of USP25 inhibitors for treating cognitive deficits and neuroinflammation in a mouse model of AD. In addition, human fetal brain tissues from the patients with DS and normal control were used to determine USP25 expression. To investigate whether trisomy 21 alters AD pathogenesis, we generated a DS-AD mouse model by crossing Dp16 mice with 5×FAD mice. In addition, BAC-Tg-USP25 mice that overexpress human $USP25$ gene were used to determine the pathological role of $USP25$ overdosage in AD pathogenesis. To discern the therapeutic potential of USP25, genetic deletion and pharmacological inhibition of USP25 were conducted in 5×FAD mice. All animal studies were performed in mice according to the protocols approved by the Institutional Animal Care and Use Committee of Xiamen University. Mice were randomly grouped by genotype, and age-matched littermates were used as controls. Experiments were conducted and analyzed in a double-blind manner, with replicates described in the figure legends. All collected data are included in the figures or supplementary figures.

Mouse strains
Sanger sequencing of PCR products was used to characterize the $USP25$ BAC clone [National Center for Biotechnology Information (NCBI) Clone DB, clone no. RP11-840D8] containing the human $USP25$ gene. Purified BAC DNA was microinjected into pronuclei of C57BL/6 fertilized oocytes and transplanted into pseudopregnant foster mothers. The transgenic offspring were screened by PCR, and BAC-Tg-USP25 mice were maintained in a C57BL/6 background. $Usp25^{-/-}$ mice were generated as previously described (19). Both Dp(16)1Yey/+ mice (stock no. 013530, referred to as Dp16 mice in this study) and 5×FAD mice (stock no. 34840-JAX) were obtained from the Jackson Laboratory (Ellsworth, ME, USA). Age-matched littermate male mice were used in the experiments except the quantitative proteomics; age-matched littermate female mice were used in the quantitative proteomics. All experiments involving animals were performed under the guidelines of the Institutional Animal Care and Use Committee of Xiamen University.

Human brain specimens
Human DS fetal brain specimens were collected and curated by the Women and Children's Hospital, School of Medicine, Xiamen University. Human studies were approved with informed consent by the ethical review board at the School of Medicine, Xiamen University (project no. XDYX2020002). Donors consisted of pregnant women

who discontinued due to congenital heart defects or trisomy 21, which was confirmed by karyotype analysis. For specimen information, see table S1.

RNA interference
Small interfering RNAs (siRNAs) were ordered from RiboBio (Guangzhou, China). The human *USP25* siRNA target sequences were as follows: si*USP25*-1: 5′-GTGAGCGATTTGCCCGAAT-3′; si*USP25*-2: 5′-GCATCAGGATTATAGGAAA-3′. The mouse *Atp6v0c* siRNA target sequence was as follows: si*Atp6v0c*: 5′-GTCCCGTTGTCCTA-GCTCG-3′. The control siRNA (siN0000001-1-5) was provided by RiboBio. siRNA was transfected into human embryonic kidney (HEK) 293T cells or primary microglia using Lipofectamine RNAi-MAX Transfection Reagent (Thermo Fisher Scientific, Carlsbad, CA, USA; 13778100).

Cell culture and transfection
Primary microglial cultures were prepared as previously described (*43*). Briefly, mixed glial cultures were acquired from WT or *Usp25*$^{-/-}$ mice on postnatal days 1 to 2, plated in flasks coated with poly-L-lysine, and grown in Dulbecco's modified Eagle's medium (DMEM) containing 10% fetal bovine serum (FBS). Granulocyte-macrophage colony-stimulating factor (25 ng ml^{-1}; R&D Systems, Minneapolis, MN, USA; 415-ML-050) was added to the cultures after 3 days. Primary microglia were harvested by shaking (200 rpm, 30 min) 10 to 12 days after plating and once every 3 days thereafter (up to four harvests). HEK293T or HeLa cells were cultured in DMEM containing 10% FBS. Once they reached an appropriate confluence, HEK293T or HeLa cells were transfected with the indicated constructs using TurboFect Transfection Reagent (Thermo Fisher Scientific, R0534).

RNA isolation and quantitative reverse transcription PCR
Total RNA was extracted using TRIzol reagent (Thermo Fisher Scientific, 15596026), and 1 μg of total RNA was reverse-transcribed into complementary DNA (cDNA) using ReverTra Ace qPCR RT Master Mix (TOYOBO, Osaka, Japan; FSQ-201). Real-time PCR was performed on the LightCycler 480 System (Roche, Mannheim, Germany) using the FastStart Universal SYBR Green Master (Roche, 04913850001). The primer sequences of target genes are included in table S2. The $2^{-\Delta\Delta Ct}$ method was used to calculate relative gene expression after normalization to the *Actb* internal control.

Immunoblot analysis
Immunoblot analysis was performed as previously described (*44*). Antibodies were used as follows: anti-USP25 (Abcam, Cambridge, MA, USA; ab187156, 1:1000), anti-APP (Millipore, Billerica, MA, USA; MAB348, 1:1000), anti-Iba1 (Wako Pure Chemical, Osaka, Japan; 016-20001, 1:500), anti-GFAP (glial fibrillary acidic protein) (Cell Signaling Technology, Danvers, MA, USA; 3670, 1:1000), anti–β-III-tubulin (Abcam, ab18207, 1:1000), anti-HA (hemagglutinin) (Sigma-Aldrich, St. Louis, MO, USA; H6908, 1:1000), anti-ubiquitin (Santa Cruz Biotechnology, Santa Cruz, CA, USA; sc-8017, 1:500), anti–β-actin (Xmbcss, Xiamen, China; bc001, 1:2000), and horse-radish peroxidase (HRP)–conjugated secondary antibodies (Thermo Fisher Scientific, 31430 or 31460; 1:3000).

Coimmunoprecipitation
Transfected HEK293T cells were lysed in lysis buffer [20 mM tris-HCl (pH 7.4), 100 mM NaCl, 1 mM EDTA, and 0.5% NP-40] sup-plemented with the Complete Protease Inhibitor Cocktail (Roche, 04693132001). Cell lysates were subjected to immunoprecipitation with antibody against Myc (Thermo Fisher Scientific, 132500, 1:200) or HA (Sigma-Aldrich, H6908, 1:200) and incubation with Dynabeads Protein G (Thermo Fisher Scientific, 10004D) followed by immunoblot analysis.

Pharmacological treatment with proteasomal and lysosomal inhibitors
HEK293T cells transfected with siUSP25 or control siRNA were incubated with lysosomal inhibitor leupeptin (100 μg ml^{-1}) (MCE, Monmouth Junction, NJ, USA; HY-18234A) or 10 μM proteasomal inhibitor MG132 (MCE, HY-13259). After 8 hours of treatment, the cells were harvested and subjected to immunoblot analysis.

Stereotactic injection of Aβ$_{42}$ oligomer
Stereotactic injection of oAβ$_{42}$ was performed as previously described (*45*, *46*). Seven-month-old *Usp25*$^{-/-}$ mice and littermate *Usp25*$^{+/+}$ mice were anesthetized, and oAβ$_{42}$ (a total of 1.5 μg in 2 μl; AnaSpec, Fremont, CA, USA; AS-20276) or control vehicle was injected bilaterally into the hippocampus using an automated stereotaxic injection apparatus (RWD Life Science, Shenzhen, China) at the following coordinates: anteroposterior, −2.2 mm from the bregma; mediolateral, ±2.0 mm; dorsoventral, −2.0 mm. Sixteen hours after injection, the mice were sacrificed and subjected to immunohistochemistry to quantify microglial migration.

Administration of AZ1
AZ1 (TubePharm, Shanghai, China) was dissolved in 5% dimethyl sulfoxide (DMSO) and +95% corn oil. Five-month-old (for LTP recordings) or 7-month-old (for behavioral tests and biochemical analyses) male 5×FAD and littermate WT mice were intraperitoneally injected with AZ1 (20 mg kg^{-1}) every day for 28 consecutive days. An equivalent amount of vehicle solvent was administered to the control group.

Pharmacokinetics of AZ1
WT ICR mice were given a single intragastric gavage of AZ1 (10 mg kg^{-1}) dissolved in 0.5% sodium carboxymethyl cellulose (CMC-Na) [containing 1% Tween 80 (pH 4.0)]. Thereafter, whole blood and brain tissues were collected at 0.5, 2, and 8 hours (*n* = 3 per group). One gram of brain tissue was homogenized in 5 ml of methanol:water (1:4, v:v), and whole blood was collected in EDTA-K$_2$ anticoagulant tubes and centrifuged at 1500*g* for 10 min at 4°C. Afterward, the supernatant was collected as plasma. Twenty-microliter aliquots of plasma and brain samples were diluted in 400 μl of acetonitrile containing internal standard (IS) [verapamil (5 ng ml^{-1}) and glibenclamide (50 ng ml^{-1})]. The mixtures were vortexed thoroughly and centrifuged at 13,000 rpm for 8 min, and then 70 μl of each supernatant was diluted in 70 μl of water. Five-microliter aliquots of the mixtures were injected into an API 4000 liquid chromatography–tandem mass spectrometry (LC-MS/MS) system (AB SCIEX, Concord, Ontario, Canada) for analysis. Positive multiple reaction monitoring (MRM) mode was used to scan the ion transitions [mass/charge ratio (*m/z*) 422.1→361.1 for AZ1 and *m/z* 455.2→165.1 for IS]. Chromatographic separation was performed using a ZORBAX XDB-C18 column (2.1 × 50-mm internal diameter and 5-μm particle size; Agilent Technologies, Santa Clara, CA, USA; column no. 50-282) at a flow rate of 0.40 ml min^{-1} in the atmospheric pressure chemical ionization (APCI) source. Mobile phase A was an aqueous solution with 0.1% formic acid; mobile phase B was

acetonitrile with 0.1% formic acid. The LC gradient was as follows: 0 to 0.50 min, 35% B; 0.50 to 1.20 min, 35 to 98% B; 1.20 to 2.20 min, 98% B; 2.20 to 2.21 min, 98 to 35% B; 3.50 min, stop.

Comprehensive metabolic panel
Mice were anaesthetized with isoflurane. Then, whole blood was collected without anticoagulant and centrifuged at 1500g for 10 min at 4°C after incubation at room temperature for 30 min. The supernatant serum was collected and then processed for the following biochemical assays: aspartate aminotransferase [International Federation of Clinical Chemistry (IFCC) method; Mindary, Shenzhen, China; 105-000443-00], alanine aminotransferase (IFCC method, Mindary, 105-000442-00), alkaline phosphatase [2-amino-2-methyl-1-propanol (AMP) buffer method, Mindary, 105-000444-00], albumin [bromocresol green (BCG) method, Mindary, 105-000450-00], total protein (biuret method, Mindary, 105-000451-00), urea [ultraviolet (UV) method, Mindary, 105-000452-00], creatinine (sarcosine oxidase method, Mindary, 105-000457-00), total cholesterol [cholesterol oxidase-peroxidase (CHOD-POD) method, Mindary, 105-000448-00], triglycerides [glycerol 3-phosphate oxidase-peroxidase (GPO-POD) method, Mindary, 105-000449-00], creatine kinase (IFCC method, Mindary, 105-000458-00), and glucose (GPO-POD method, Mindary, 105-000949-00). Spectrophotometric readings were obtained with the BS-240 Clinical Chemistry Analyzer (Mindary).

Immunocytochemistry
Cells were plated on coverslips coated with poly-L-lysine, fixed with 4% paraformaldehyde at room temperature for 20 min, and then permeabilized with 0.2% Triton X-100 in phosphate-buffered saline for 5 min. After blocking, the cells were subjected to immunostaining with the indicated primary antibodies at 4°C overnight, stained with Alexa Fluor 488– and Alexa Fluor 594–conjugated secondary antibodies (Thermo Fisher Scientific, A11001, A11005, A11008, and A11012; 1:500), and counterstained with 4′,6-diamidino-2-phenylindole (DAPI; Sigma-Aldrich, D95542; 1 μg ml^{-1}). The following primary antibodies were used: anti-Iba1 (Wako Pure Chemical, 019-19741; 1:200), anti-Myc (Thermo Fisher Scientific, 132500; 1:500), and anti-HA (Sigma-Aldrich, H6908; 1:500). Confocal images were acquired with a Leica SP8 confocal microscope and subjected to quantification with ImageJ software [National Institutes of Health (NIH)].

Immunohistochemistry
Perfusion and brain slice preparation were performed as previously described (44). Brain slices were stained using the following primary antibodies: anti-Iba1 (Wako Pure Chemical, 019-19741; 1:500), anti-CD68 (Bio-Rad, Hercules, CA, USA; MCA1957, 1:100), anti-PSD95 (Millipore, MAB1596; 1:100), and 6E10 (BioLegend, San Diego, CA, USA; 803001; 1:400). Alexa Fluor 488– and Alexa Fluor 594–conjugated secondary antibodies (Thermo Fisher Scientific, A11001, A11005, A11008, or A11012; 1:500) were used, and then the slices were counterstained with DAPI (Sigma-Aldrich, D95542; 1 μg ml^{-1}). Z-stack confocal images were acquired with a Leica SP8 confocal microscope. The number and somatic size of Iba1$^+$ cells were manually counted using ImageJ software (NIH), and lengths of Iba1$^+$ cell processes were analyzed using the Filament function in the Imaris software (Bitplane, Belfast, UK; version 9.2.0). To analyze synapse elimination by microglia, z-stack images were acquired from slices coimmunostained with anti-PSD95 and anti-Iba1 antibodies, and the volumes of microglia and PSD95$^+$ synapses were reconstructed using the Surfaces function in the Imaris software (Bitplane, version 9.2.0).

Golgi staining
Mice were anesthetized, and brains were collected for Golgi staining using the FD Rapid Golgi Stain Kit (FD Neuro Technologies, Columbia, MD, USA; PK401), according to the manufacturer's protocol. Z-stack images were acquired with a laser scanning confocal microscope (Olympus FV1000), and spine density was quantified using ImageJ software (NIH).

Synaptosome purification and phagocytosis assay
Synaptosomes were purified as previously described (47) and conjugated with pHrodo Red dye (Thermo Fisher Scientific, P36600) in Na$_2$CO$_3$ at room temperature for 2 hours (48). Unbound pHrodo Red dye was washed out with Dulbecco's phosphate-buffered saline (DPBS). $Usp25^{+/+}$ and $Usp25^{-/-}$ microglia were plated at a density of 2×10^5 cell per well and then incubated with 5 μl of pHrodo Red dye–conjugated synaptosomes in the presence or absence of 10 μM oAβ$_{42}$ (AnaSpec, AS-20276). Twenty-four hours after incubation, microglia were subjected to immunocytochemistry.

RNA-seq analysis
Total RNA was extracted from hippocampus using TRIzol reagent (Thermo Fisher Scientific, 15596026). After qualification using an Agilent 2100 Bioanalyzer system (Agilent Technologies), the total RNA was subjected to sequencing library preparation using the NEBNext Ultra RNA Library Prep Kit for Illumina (NEB, Ipswich, MA, USA; E7530) according to the manufacturer's recommendations, followed by clustering, which was performed on the cBot Cluster Generation System (Illumina, San Diego, CA, USA) using the TruSeq PE Cluster Kit v3-cBot-HS (Illumina, PE-401-3001). Sequencing was performed on the Illumina NovaSeq 6000 or HiSeq 4000 System, and 150–base pair (bp) paired-end reads were generated.

Raw RNA-seq reads were aligned to the Ensembl mouse reference genome GRCm38 (mm10) using HISAT2 (version 2.0.5) (49). Gene expression was subsequently quantified using featureCounts (version 1.5.0-p3) (50). Then, the raw gene counts were processed with the DESeq2 package (version 1.26.0) (51) in R (version 3.6.1) to analyze DEGs. GO enrichment analysis of DEGs was performed in R using the package clusterProfiler (version 3.14.3, qvalueCutoff = 0.05) (52).

The WGCNA (53) systematic biological method for describing the correlation patterns of genes among different samples was performed using the WGCNA package (version 1.69) (54) to identify unsigned gene coexpression networks and modules. First, gene modules were identified with similar gene expression patterns using hierarchical clustering. For each gene module, the expression matrix of the genes contained in the module was extracted and then the first principal component (PCA1) was calculated as "module eigengene." In addition, the Pearson correlation between the module eigengene of each sample and different genotypes of each sample were analyzed. Numbers in the heatmap represent the Pearson correlation and corresponding P values. Sample traits, including among the sample groups, were correlated to genes and modules, and significantly correlated modules were determined by $P < 0.05$. Eigengenes in each module that were significantly correlated with sample traits were selected by $P < 0.05$.

TMT-based quantitative proteomics
The cerebral cortices and hippocampi of 6-month-old female 5×FAD, 5×FAD;$Usp25^{-/-}$, and littermate WT mice were lysed in 6 M guanidine hydrochloride, homogenized with a homogenizer (MP Biomedicals,

Irvine, CA, USA), sonicated, and then boiled for 10 min. After centrifugation, the supernatants were processed for filter-aided sample preparation (FASP) digestion using trypsin, and then 100 µg of the peptide mixture from each sample was labeled using TMT 10plex Isobaric Label Reagent (Thermo Fisher Scientific, 90110) according to the manufacturer's instructions. The TMT-labeled digested samples were separated into 15 fractions using the Pierce High pH Reversed-Phase Peptide Fractionation Kit (Thermo Fisher Scientific, 84868). Each fraction was separated with EASY-nLC 1000 Liquid Chromatograph (Thermo Fisher Scientific) and then subjected to LC-MS/MS analysis on Q Exactive HF-X Hybrid Quadrupole-Orbitrap Mass Spectrometer (Thermo Fisher Scientific) for 90 min. The spectra were analyzed by Proteome Discoverer (Thermo Fisher Scientific, version 1.4) and then subjected to a database search using the MASCOT search engine (Matrix Science, Boston, MA, USA; version 2.2) for peptide identification. All identified proteins were determined using a false discovery rate (FDR) threshold of <0.01. After retrieval from the UniProtKB database and searching against the SwissProt database (mouse), the top BLAST hits were processed for GO enrichment analysis using Blast2GO (BioBam, Valencia, Spain; version 3.3.5).

Electrophysiology

Electrophysiology was performed as previously described (44). Mice were anesthetized with isoflurane, and then the brains were rapidly removed, placed in ice-cold artificial cerebrospinal fluid [ACSF; 120 mM sucrose, 2.5 mM KCl, 10 mM $MgSO_4$, 1.25 mM NaH_2PO_4, 26 mM $NaHCO_3$, 10 mM D-glucose, 64 mM NaCl, and 0.5 mM $CaCl_2$ (pH 7.4), ~310 mOsm], and bubbled with carbogen (95% O_2 + 5% CO_2). Brain slices were cut (400 µm thick) using a Leica VT1200S vibratome, incubated in ACSF [3.5 mM KCl, 120 mM NaCl, 1.3 mM $MgSO_4$, 10 mM D-glucose, 1.25 mM NaH_2PO_4, 26 mM $NaHCO_3$, and 2.5 mM $CaCl_2$ (pH 7.4), ~300 mOsm], and bubbled with carbogen (95% O_2 + 5% CO_2) at 32°C for 1 hour. The slices recovered at room temperature for at least 1 hour before recording. For LTP recording, the Schaffer collateral inputs to the CA1 region were stimulated with a bipolar tungsten electrical stimulating electrode, while field excitatory postsynaptic potentials (fEPSPs) were recorded from the dendritic layer in the Schaffer collateral pathway. Baseline responses were acquired every 20 s with a stimulation intensity that yielded 30% of the maximum response. After a 20-min stable baseline recording, LTP was induced by high-frequency stimulation (two trains of 100-Hz stimuli with an interval of 30 s), followed by continued recording for 60 min.

For mEPSC and mIPSC recordings, brain slices were incubated in ACSF [2.5 mM KCl, 126 mM NaCl, 2.4 mM $MgCl_2$, 1.2 mM $CaCl_2$, 1.2 mM NaH_2PO_4, 11 mM D-glucose, and 18 mM $NaHCO_3$ (pH 7.4), ~300 mOsm], bubbled with carbogen (95% O_2 + 5% CO_2), and kept at 32°C. Tetrodotoxin (1 µM) was added to the perfusion ACSF to block sodium channels. A glass pipette was filled with a solution containing 2 mM $MgCl_2 \cdot 6H_2O$, 140 mM $CsCH_3SO_3$, 5 mM TEA-Cl, 1 mM EGTA, 2.5 mM Mg-ATP (adenosine triphosphate), and 0.3 mM Na-GTP (guanosine triphosphate) (pH 7.3, ~290 mOsm), and the resistance of the pipette was 5 to 8 megohms. The pipette was placed in dentate gyrus (DG) granule neurons, and recordings were obtained at a holding potential of −70 mV for mEPSCs and 0 mV for mIPSCs. The resistance of the pipette was 5 to 8 megohms. Data were acquired with a Multiclamp 700B patch-clamp amplifier (Molecular Devices, San Jose, CA, USA), filtered at 2 kHz, and sampled at 10 kHz, followed by processing for analysis using pClamp software (Molecular Devices, version 10.6).

Y-maze test

Experimental mice were placed in the center of a Y-shaped maze with three arms at 120° from each other and allowed to freely explore the three arms for 5 min. The percentage of spontaneous alternation was calculated automatically using Smart Video Tracking Software 3.0 (Panlab, Harvard Apparatus, Holliston, MA, USA).

MWM test

MWM tests were conducted in a circular tank (diameter of 120 cm) filled with opaque water kept at 22°C, using a modified protocol (55). Four bright and contrasting shapes, which served as reference cues, were affixed to the walls surrounding the tank. A fixed platform (diameter of 10 cm) was submerged 1 cm below the surface of the water in the target quadrant. On the training days, the mice were placed into the maze at one of four random points, and two trials were performed every day for six consecutive days. Mice were allowed to search for the hidden platform for 60 s. If a mouse was unable to find the platform within 60 s, it was guided to the platform and kept there for another 10 s. The latency to reach the hidden platform was scored by Smart Video Tracking Software 3.0 (Panlab, Harvard Apparatus). On day 7 after training, the platform was removed, and a probe test was performed. The time spent in each quadrant was recorded.

FC test

FC was performed using a modified protocol (56, 57). Experimental mice were placed in a conditioning chamber (Panlab, Harvard Apparatus) and allowed to freely explore the chamber for 2 min. Thereafter, a 60-dB white noise stimulus was presented for 30 s as a conditioned stimulus (CS), and a 0.5-mA foot shock was given to the mice as an unconditioned stimulus (US) during the last 2 s of the noise. The CS-US pair was presented three times at 1-min intervals. Mice were removed 1 min after the last CS-US pair. For the contextual test, the mice were placed in the same conditioning chamber 24 hours after training, and freezing behaviors were scored for 5 min. For the cued test, the mice were placed in another testing chamber with a novel contextual environment for 3 min, and thereafter, a CS was presented for 3 min.

Statistical analysis

All the data were collected and analyzed in a double-blind manner. Statistical analyses were performed using GraphPad Prism software (GraphPad Software, La Jolla, CA, USA; version 8). The data distribution was assessed by the Shapiro-Wilk normality test. The statistical methods used to analyze the quantitative data are described in the figure legends. All data represent means ± SEM. P values of <0.05 were considered statistically significant.

SUPPLEMENTARY MATERIALS

Supplementary material for this article is available at http://advances.sciencemag.org/cgi/content/full/7/1/eabe1340/DC1

REFERENCES AND NOTES

1. S. E. Antonarakis, B. G. Skotko, M. S. Rafii, A. Strydom, S. E. Pape, D. W. Bianchi, S. L. Sherman, R. H. Reeves, Down syndrome. *Nat. Rev. Dis. Primers* **6**, 9 (2020).
2. S. E. Antonarakis, Down syndrome and the complexity of genome dosage imbalance. *Nat. Rev. Genet.* **18**, 147–163 (2017).
3. F. K. Wiseman, T. Al-Janabi, J. Hardy, A. Karmiloff-Smith, D. Nizetic, V. L. J. Tybulewicz, E. M. C. Fisher, A. Strydom, A genetic cause of Alzheimer disease: Mechanistic insights from Down syndrome. *Nat. Rev. Neurosci.* **16**, 564–574 (2015).

4. K. E. Wisniewski, A. J. Dalton, C. McLachlan, G. Y. Wen, H. M. Wisniewski, Alzheimer's disease in Down's syndrome: Clinicopathologic studies. *Neurology* **35**, 957–961 (1985).

5. J. B. Leverenz, M. A. Raskind, Early amyloid deposition in the medial temporal lobe of young Down syndrome patients: A regional quantitative analysis. *Exp. Neurol.* **150**, 296–304 (1998).

6. Q. Li, B. A. Barres, Microglia and macrophages in brain homeostasis and disease. *Nat. Rev. Immunol.* **18**, 225–242 (2018).

7. M. Colonna, O. Butovsky, Microglia function in the central nervous system during health and neurodegeneration. *Annu. Rev. Immunol.* **35**, 441–468 (2017).

8. S. Hong, V. F. Beja-Glasser, B. M. Nfonoyim, A. Frouin, S. Li, S. Ramakrishnan, K. M. Merry, Q. Shi, A. Rosenthal, B. A. Barres, C. A. Lemere, D. J. Selkoe, B. Stevens, Complement and microglia mediate early synapse loss in Alzheimer mouse models. *Science* **352**, 712–716 (2016).

9. B. L. Heckmann, B. J. W. Teubner, B. Tummers, E. Boada-Romero, L. Harris, M. Yang, C. S. Guy, S. S. Zakharenko, D. R. Green, LC3-associated endocytosis facilitates β-amyloid clearance and mitigates neurodegeneration in murine Alzheimer's disease. *Cell* **178**, 536–551.e14 (2019).

10. M. A. DeTure, D. W. Dickson, The neuropathological diagnosis of Alzheimer's disease. *Mol. Neurodegener.* **14**, 32 (2019).

11. X. Zhou, S. Wahane, M.-S. Friedl, M. Kluge, C. C. Friedel, K. Avrampou, V. Zachariou, L. Guo, B. Zhang, X. He, R. H. Friedel, H. Zou, Microglia and macrophages promote corralling, wound compaction and recovery after spinal cord injury via Plexin-B2. *Nat. Neurosci.* **23**, 337–350 (2020).

12. A. Otxoa-de-Amezaga, F. Miró-Mur, J. Pedragosa, M. Gallizioli, C. Justicia, N. Gaja-Capdevila, F. Ruíz-Jaen, A. Salas-Perdomo, A. Bosch, M. Calvo, L. Marquez-Kisinousky, A. Denes, M. Gunzer, A. M. Planas, Microglial cell loss after ischemic stroke favors brain neutrophil accumulation. *Acta Neuropathol.* **137**, 321–341 (2019).

13. C. Ising, C. Venegas, S. Zhang, H. Scheiblich, S. V. Schmidt, A. Vieira-Saecker, S. Schwartz, S. Albasset, R. M. McManus, D. Tejera, A. Griep, F. Santarelli, F. Brosseron, S. Opitz, J. Stunden, M. Merten, R. Kayed, D. T. Golenbock, D. Blum, E. Latz, L. Buée, M. T. Heneka, NLRP3 inflammasome activation drives tau pathology. *Nature* **575**, 669–673 (2019).

14. F. C. Bennett, S. A. Liddelow, Microglia metabolic breakdown drives Alzheimer's pathology. *Cell Metab.* **30**, 405–406 (2019).

15. M. Gratuze, C. E. G. Leyns, D. M. Holtzman, New insights into the role of TREM2 in Alzheimer's disease. *Mol. Neurodegener.* **13**, 66 (2018).

16. C. Pohl, I. Dikic, Cellular quality control by the ubiquitin-proteasome system and autophagy. *Science* **366**, 818–822 (2019).

17. Q. Zheng, T. Huang, L. Zhang, Y. Zhou, H. Luo, H. Xu, X. Wang, Dysregulation of ubiquitin-proteasome system in neurodegenerative diseases. *Front. Aging Neurosci.* **8**, 303 (2016).

18. R. Valero, G. Marfany, O. González-Angulo, G. González-González, L. Puelles, R. González-Duarte, *USP25*, a novel gene encoding a deubiquitinating enzyme, is located in the gene-poor region 21q11.2. *Genomics* **62**, 395–405 (1999).

19. B. Zhong, X. Liu, X. Wang, S. H. Chang, X. Liu, A. Wang, J. M. Reynolds, C. Dong, Negative regulation of IL-17-mediated signaling and inflammation by the ubiquitin-specific protease USP25. *Nat. Immunol.* **13**, 1110–1117 (2012).

20. B. Zhong, X. Liu, X. Wang, X. Liu, H. Li, B. G. Darnay, X. Lin, S.-C. Sun, C. Dong, Ubiquitin-specific protease 25 regulates TLR4-dependent innate immune responses through deubiquitination of the adaptor protein TRAF3. *Sci. Signal.* **6**, ra35 (2013).

21. Z. Li, T. Yu, M. Morishima, A. Pao, J. LaDuca, J. Conroy, N. Nowak, S.-I. Matsui, I. Shiraishi, Y. E. Yu, Duplication of the entire 22.9 Mb human chromosome 21 syntenic region on mouse chromosome 16 causes cardiovascular and gastrointestinal abnormalities. *Hum. Mol. Genet.* **16**, 1359–1366 (2007).

22. T. Yu, C. Liu, P. Belichenko, S. J. Clapcote, S. Li, A. Pao, A. Kleschevnikov, A. R. Bechard, S. Asrar, R. Chen, N. Fan, Z. Zhou, Z. Jia, C. Chen, J. C. Roder, B. Liu, A. Baldini, W. C. Mobley, Y. E. Yu, Effects of individual segmental trisomies of human chromosome 21 syntenic regions on hippocampal long-term potentiation and cognitive behaviors in mice. *Brain Res.* **1366**, 162–171 (2010).

23. H. Oakley, S. L. Cole, S. Logan, E. Maus, P. Shao, J. Craft, A. Guillozet-Bongaarts, M. Ohno, J. Disterhoft, L. Van Eldik, R. Berry, R. Vassar, Intraneuronal β-amyloid aggregates, neurodegeneration, and neuron loss in transgenic mice with five familial Alzheimer's disease mutations: Potential factors in amyloid plaque formation. *J. Neurosci.* **26**, 10129–10140 (2006).

24. Y.-H. Hu, Y. Zhang, L.-Q. Jiang, S. Wang, C.-Q. Lei, M.-S. Sun, H.-B. Shu, Y. Liu, WDFY1 mediates TLR3/4 signaling by recruiting TRIF. *EMBO Rep.* **16**, 447–455 (2015).

25. J. D. Wrigley, G. Gavory, I. Simpson, M. Preston, H. Plant, J. Bradley, A. U. Goeppert, E. Rozycka, G. Davies, J. Walsh, A. Valentine, K. McClelland, K. E. Odrzywol, J. Renshaw, J. Boros, J. Tart, L. Leach, T. Nowak, R. A. Ward, T. Harrison, D. M. Andrews, Identification and characterization of dual inhibitors of the USP25/28 deubiquitinating enzyme subfamily. *ACS Chem. Biol.* **12**, 3113–3125 (2017).

26. M. T. Heneka, M. J. Carson, J. El Khoury, G. E. Landreth, F. Brosseron, D. L. Feinstein, A. H. Jacobs, T. Wyss-Coray, J. Vitorica, R. M. Ransohoff, K. Herrup, S. A. Frautschy, B. Finsen, G. C. Brown, A. Verkhratsky, K. Yamanaka, J. Koistinaho, E. Latz, A. Halle, G. C. Petzold, T. Town, D. Morgan, M. L. Shinohara, V. H. Perry, C. Holmes, N. G. Bazan, D. J. Brooks, S. Hunot, B. Joseph, N. Deigendesch, O. Garaschuk, E. Boddeke, C. A. Dinarello, J. C. Breitner, G. M. Cole, D. T. Golenbock, M. P. Kummer, Neuroinflammation in Alzheimer's disease. *Lancet Neurol.* **14**, 388–405 (2015).

27. D. M. Wilcock, W. S. T. Griffin, Down's syndrome, neuroinflammation, and Alzheimer neuropathogenesis. *J. Neuroinflammation* **10**, 84 (2013).

28. T. Guo, D. Zhang, Y. Zeng, T. Y. Huang, H. Xu, Y. Zhao, Molecular and cellular mechanisms underlying the pathogenesis of Alzheimer's disease. *Mol. Neurodegener.* **15**, 40 (2020).

29. R. S. Pandey, L. Graham, A. Uyar, C. Preuss, G. R. Howell, G. W. Carter, Genetic perturbations of disease risk genes in mice capture transcriptomic signatures of late-onset Alzheimer's disease. *Mol. Neurodegener.* **14**, 50 (2019).

30. D. K. Kim, J. Park, D. Han, J. Yang, A. Kim, J. Woo, Y. Kim, I. Mook-Jung, Molecular and functional signatures in a novel Alzheimer's disease mouse model assessed by quantitative proteomics. *Mol. Neurodegener.* **13**, 2 (2018).

31. A. Bosch-Comas, K. Lindsten, R. Gonzàlez-Duarte, M. G. Masucci, G. Marfany, The ubiquitin-specific protease USP25 interacts with three sarcomeric proteins. *Cell. Mol. Life Sci.* **63**, 723–734 (2006).

32. F. K. Wiseman, L. J. Pulford, C. Barkus, F. Liao, E. Portelius, R. Webb, L. Chávez-Gutiérrez, K. Cleverley, S. Noy, O. Sheppard, T. Collins, C. Powell, C. J. Sarell, M. Rickman, X. Choong, J. L. Tosh, C. Siganporia, H. T. Whittaker, F. Stewart, M. Szaruga, M. P. Murphy, K. Blennow, B. de Strooper, H. Zetterberg, D. Bannerman, D. M. Holtzman, V. L. J. Tybulewicz, E. M. C. Fisher, Trisomy of human chromosome 21 enhances amyloid-β deposition independently of an extra copy of *APP*. *Brain* **141**, 2457–2474 (2018).

33. E. W. Wolvetang, O. M. Bradfield, M. Tymms, S. Zavarsek, T. Hatzistavrou, I. Kola, P. J. Hertzog, The chromosome 21 transcription factor ETS2 transactivates the β-*APP* promoter: Implications for Down syndrome. *Biochim. Biophys. Acta* **1628**, 105–110 (2003).

34. Y. Li, H. Wang, S. Wang, D. Quon, Y.-W. Liu, B. Cordell, Positive and negative regulation of APP amyloidogenesis by sumoylation. *Proc. Natl. Acad. Sci. U.S.A.* **100**, 259–264 (2003).

35. S. R. Ryoo, H.-J. Cho, H.-W. Lee, H. K. Jeong, C. Radnaabazar, Y.-S. Kim, M.-J. Kim, M.-Y. Son, H. Seo, S.-H. Chung, W.-J. Song, Dual-specificity tyrosine(Y)-phosphorylation regulated kinase 1A-mediated phosphorylation of amyloid precursor protein: Evidence for a functional link between Down syndrome and Alzheimer's disease. *J. Neurochem.* **104**, 1333–1344 (2008).

36. K. Y. Mok, E. L. Jones, M. Hanney, D. Harold, R. Sims, J. Williams, C. Ballard, J. Hardy, Polymorphisms in *BACE2* may affect the age of onset Alzheimer's dementia in Down syndrome. *Neurobiol. Aging* **35**, 1513.e1-5 (2014).

37. S. Mueller-Steiner, Y. Zhou, H. Arai, E. D. Roberson, B. Sun, J. Chen, X. Wang, G. Yu, L. Esposito, L. Mucke, L. Gan, Antiamyloidogenic and neuroprotective functions of cathepsin B: Implications for Alzheimer's disease. *Neuron* **51**, 703–714 (2006).

38. B. Readhead, J.-V. Haure-Mirande, D. Mastroeni, M. Audrain, T. Fanutza, S. H. Kim, R. D. Blitzer, S. Gandy, J. T. Dudley, M. E. Ehrlich, miR155 regulation of behavior, neuropathology, and cortical transcriptomics in Alzheimer's disease. *Acta Neuropathol.* **140**, 295–315 (2020).

39. C. K. Glass, K. Saijo, B. Winner, M. C. Marchetto, F. H. Gage, Mechanisms underlying inflammation in neurodegeneration. *Cell* **140**, 918–934 (2010).

40. A. D. Thome, A. Faridar, D. R. Beers, J. R. Thonhoff, W. Zhao, S. Wen, B. Pascual, J. C. Masdeu, S. H. Appel, Functional alterations of myeloid cells during the course of Alzheimer's disease. *Mol. Neurodegener.* **13**, 61 (2018).

41. A. Litvinchuk, Y.-W. Wan, D. B. Swartzlander, F. Chen, A. Cole, N. E. Propson, Q. Wang, B. Zhang, Z. Liu, H. Zheng, Complement C3aR inactivation attenuates tau pathology and reverses an immune network deregulated in tauopathy models and Alzheimer's disease. *Neuron* **100**, 1337–1353.e5 (2018).

42. F. L. Heppner, R. M. Ransohoff, B. Becher, Immune attack: The role of inflammation in Alzheimer disease. *Nat. Rev. Neurosci.* **16**, 358–372 (2015).

43. L. Zhong, Y. Xu, R. Zhuo, T. Wang, K. Wang, R. Huang, D. Wang, Y. Gao, Y. Zhu, X. Sheng, K. Chen, N. Wang, L. Zhu, D. Can, Y. Marten, M. Shinohara, C.-C. Liu, D. Du, H. Sun, L. Wen, H. Xu, G. Bu, X.-F. Chen, Soluble TREM2 ameliorates pathological phenotypes by modulating microglial functions in an Alzheimer's disease model. *Nat. Commun.* **10**, 1365 (2019).

44. F. Zeng, X. Ma, L. Zhu, Q. Xu, Y. Zeng, Y. Gao, G. Li, T. Guo, H. Zhang, X. Tang, Z. Wang, Z. Ye, L. Zheng, H. Zhang, Q. Zheng, K. Li, J. Lu, X. Qi, H. Luo, X. Zhang, Z. Wang, Y. Zhou, Y. Yao, R. Ke, Y. Zhou, Y. Liu, H. Sun, T. Huang, Z. Shao, H. Xu, X. Wang, The deubiquitinase USP6 affects memory and synaptic plasticity through modulating NMDA receptor stability. *PLOS Biol.* **17**, e3000525 (2019).

45. Y. Zhao, X. Wu, X. Li, L.-L. Jiang, X. Gui, Y. Liu, Y. Sun, B. Zhu, J. C. Piña-Crespo, M. Zhang, N. Zhang, X. Chen, G. Bu, Z. An, T. Y. Huang, H. Xu, TREM2 is a receptor for β-Amyloid that mediates microglial function. *Neuron* **97**, 1023–1031.e7 (2018).

46. L. Zhong, Z. Wang, D. Wang, Z. Wang, Y. A. Martens, L. Wu, Y. Xu, K. Wang, J. Li, R. Huang, D. Can, H. Xu, G. Bu, X.-F. Chen, Amyloid-beta modulates microglial responses by binding to the triggering receptor expressed on myeloid cells 2 (TREM2). *Mol. Neurodegener.* **13**, 15 (2018).

47. P. R. Dunkley, P. E. Jarvie, P. J. Robinson, A rapid Percoll gradient procedure for preparation of synaptosomes. *Nat. Protoc.* **3**, 1718–1728 (2008).

48. Y. G. Byun, W.-S. Chung, A novel *in vitro* live-imaging assay of astrocyte-mediated phagocytosis using pH indicator-conjugated synaptosomes. *J. Vis. Exp.* **132**, 56647 (2018).

49. D. Kim, J. M. Paggi, C. Park, C. Bennett, S. L. Salzberg, Graph-based genome alignment and genotyping with HISAT2 and HISAT-genotype. *Nat. Biotechnol.* **37**, 907–915 (2019).

50. Y. Liao, G. K. Smyth, W. Shi, featureCounts: An efficient general purpose program for assigning sequence reads to genomic features. *Bioinformatics* **30**, 923–930 (2014).

51. M. I. Love, W. Huber, S. Anders, Moderated estimation of fold change and dispersion for RNA-seq data with DESeq2. *Genome Biol.* **15**, 550 (2014).

52. G. Yu, L.-G. Wang, Y. Han, Q.-Y. He, clusterProfiler: An R package for comparing biological themes among gene clusters. *OMICS* **16**, 284–287 (2012).

53. B. Zhang, S. Horvath, A general framework for weighted gene co-expression network analysis. *Stat. Appl. Genet. Mol. Biol.* **4**, Article17 (2005).

54. P. Langfelder, S. Horvath, WGCNA: An R package for weighted correlation network analysis. *BMC Bioinformatics* **9**, 559 (2008).

55. J. Seo, P. Giusti-Rodriguez, Y. Zhou, A. Rudenko, S. Cho, K. T. Ota, C. Park, H. Patzke, R. Madabhushi, L. Pan, A. E. Mungenast, J.-S. Guan, I. Delalle, L.-H. Tsai, Activity-dependent p25 generation regulates synaptic plasticity and Aβ-induced cognitive impairment. *Cell* **157**, 486–498 (2014).

56. C.-C. Liu, C.-W. Tsai, F. Deak, J. Rogers, M. Penuliar, Y. M. Sung, J. N. Maher, Y. Fu, X. Li, H. Xu, S. Estus, H.-S. Hoe, J. D. Fryer, T. Kanekiyo, G. Bu, Deficiency in LRP6-mediated Wnt signaling contributes to synaptic abnormalities and amyloid pathology in Alzheimer's disease. *Neuron* **84**, 63–77 (2014).

57. H. Shoji, K. Takao, S. Hattori, T. Miyakawa, Contextual and cued fear conditioning test using a video analyzing system in mice. *J. Vis. Exp.* **85**, 50871 (2014).

Citation: Q. Zheng, G. Li, S. Wang, Y. Zhou, K. Liu, Y. Gao, Y. Zhou, L. Zheng, L. Zhu, Q. Deng, M. Wu, A. Di, L. Zhang, Y. Zhao, H. Zhang, H. Sun, C. Dong, H. Xu, X. Wang, Trisomy 21–induced dysregulation of microglial homeostasis in Alzheimer's brains is mediated by USP25. *Sci. Adv.* **7**, eabe1340 (2021).

ScienceAdvances

Trisomy 21–induced dysregulation of microglial homeostasis in Alzheimer's brains is mediated by USP25

Qiuyang ZhengGuilin LiShihua WangYing ZhouKe LiuYue GaoYulin ZhouLiangkai ZhengLin ZhuQingfang DengMeiling WuAnjie DiLishan ZhangYingjun ZhaoHongfeng ZhangHao SunChen DongHuaxi XuXin Wang

View the article online
https://www.science.org/doi/10.1126/sciadv.abe1340
Permissions
https://www.science.org/help/reprints-and-permissions

Use of this article is subject to the Terms of service